



Template-free preparation of macro/mesoporous g-C₃N₄/TiO₂ heterojunction photocatalysts with enhanced visible light photocatalytic activity

Ruirui Hao ^{a,b}, Guohong Wang ^{a,b,*}, Hua Tang ^c, Lingling Sun ^{a,b}, Chang Xu ^{a,b}, Deyan Han ^{a,b}

^a Hubei Collaborative Innovation Center for Rare Metal Chemistry, Hubei Normal University, Huangshi 435002, PR China

^b Hubei Key Laboratory of Pollutant Analysis and Reuse Technology, Hubei Normal University, Huangshi 435002, PR China

^c School of Materials Science and Engineering, Jiangsu University, Zhenjiang 212013, PR China



ARTICLE INFO

Article history:

Received 4 November 2015

Received in revised form 1 January 2016

Accepted 11 January 2016

Available online 15 January 2016

Keywords:

Template-free
Macro/mesoporous
Heterojunction
Visible light
g-C₃N₄/TiO₂
Photocatalytic activity

ABSTRACT

Mesoporous photocatalytic materials with macroporous structures have attracted more and more attention because of their textural mesopores and intrinsic interconnected pore networks, which are able to efficiently transport guest species to framework binding sites. In this work, macro/mesoporous g-C₃N₄/TiO₂ heterojunction photocatalysts were fabricated without templates or additives by a facile calcination method using tetrabutyl titanate and melamine as the feedstocks. Photocatalytic experiments of the as-prepared samples were measured by the photocatalytic oxidation degradation of RhB solution at room temperature under visible light irradiation. The results indicated that the melamine content in the precursors had an important influence on photocatalytic activity of the as-prepared samples. At the optimal loading content, the apparent reaction rate constant (*k*) was $47.8 \times 10^{-3} \text{ min}^{-1}$ for RhB degradation, exceeding that of pure TiO₂ ($6.6 \times 10^{-3} \text{ min}^{-1}$) and g-C₃N₄ ($15.2 \times 10^{-3} \text{ min}^{-1}$) by factor of 7.2 and 3.1 respectively. The improved photocatalytic activity was attributed to high surface area and heterostructure formation of g-C₃N₄/TiO₂ composites. The trapping experiment results showed that •O₂⁻ and h⁺ were main active species in the decomposition of RhB. A possible enhanced photocatalytic mechanism of g-C₃N₄/TiO₂ heterojunction photocatalysts was proposed.

© 2016 Elsevier B.V. All rights reserved.

1. Introduction

The utilization of semiconductor photocatalysts for the decomposition of organic pollutions has been regarded as an efficient method to solve environmental pollution problems [1–4]. Among various oxide semiconductor photocatalysts, TiO₂ was regarded as a promising material for widespread environmental applications due to their particular performance such as strong oxidizing power, chemical stability, low cost and non-toxic [5–7]. Nevertheless, the photocatalytic performance of titania must be further enhanced owing to the fast recombination rate of the photo-generated electron-hole pairs within the TiO₂ particles and the restricted UV-light response (only about 4% of total sunlight) [8,9]. To date, numerous effective strategies were developed to extend

the response range from UV to visible light and improve the visible light photocatalytic activity of TiO₂, such as noble metal depositing [10,11], metal and non-metal ion doping [12–14], semiconductor coupling [15–17], surface sensitization [18], and so on. Among them, semiconductor coupling has been an efficient method to improve visible light photocatalytic activity of TiO₂ and attracted widespread interest owing to the formation of a close interface between two semiconductor materials [19–23]. This special structure can promote the separation of the photoinduced hole-electron pairs, hence resulting in improved visible light photocatalytic activity [24,25].

g-C₃N₄ has been proved to be a non-toxic, stable and facile organic semiconductor photocatalysts [26–28]. The band gap of g-C₃N₄ is approximately 2.7 eV, which exhibits a strong response for the visible-light region [29–31]. In addition, g-C₃N₄ was easily obtained by mild thermolysis routes from inexpensive nitrogen-rich precursors such as urea, melamine, thiourea, cyanamide and dicyandiamide [32–34]. Recent results show that the hybridization of TiO₂ with g-C₃N₄ displays an enhanced photocatalytic

* Corresponding author at: Hubei Collaborative Innovation Center for Rare Metal Chemistry, Hubei Normal University, Huangshi 435002, PR China.

E-mail address: wanggh2003@163.com (G. Wang).

activity because of the unique heterojunction structure [35–38]. Therefore, the preparation of g-C₃N₄/TiO₂ heterojunction photocatalyst is a promising strategy to improve charge separation and enhance photocatalytic performance of TiO₂ [39,40]. For example, Zhang et al. [41] confirmed that heterojunctions in g-C₃N₄/TiO₂ (B) nanofibres with exposed (001) plane showed superior photocatalytic performance in decomposition of RhB solution under visible light illumination. The enhanced activities of the g-C₃N₄/TiO₂ heterojunction photocatalysts relied on stable interfacial structure between g-C₃N₄ and the plane (110) of TiO₂ (B). Wang et al. [42] demonstrated that g-C₃N₄/P25 heterojunction photocatalysts showed higher photocatalytic performance toward degradation phenol and RhB. Huang et al. [43] reported that the photocatalytic activity of g-C₃N₄/TiO₂-HNB heterojunction photocatalysts was greatly improved via (101) facets because of efficient removal of photoinduced electrons accumulate on (101) facets of TiO₂.

Mesoporous photocatalytic materials with macroporous structures have attracted more and more attention because of their textural mesopores and intrinsic interconnected pore networks, which are able to efficiently transport guest species to framework binding sites. The macro/mesoporous structures are beneficial for the increase in the specific surface area, thereby offering more active sites for photocatalytic reaction. In our work, the g-C₃N₄/TiO₂ heterojunction photocatalysts were prepared by a facile calcination method using tetrabutyl titanate and melamine as the feedstocks. The as-prepared g-C₃N₄/TiO₂ heterojunction photocatalysts have large specific surface area than pure TiO₂ (34.8 m²/g) and pure g-C₃N₄ (14.3 m²/g). Moreover, the close interface contact between TiO₂ and g-C₃N₄ inhibited the fast recombination of electron-hole pairs, resulting in an enhanced visible light photocatalytic activity for the degradation of RhB. To the best of our knowledge, this work is the first report about macro/mesoporous g-C₃N₄/TiO₂ heterojunction photocatalysts for decomposition of RhB at room temperature under visible light irradiation. The present work may provide a new insight for the smart design and synthesis of various highly efficient photocatalysts for environmental and energy applications.

2. Experimental

2.1. Materials

All raw materials used in this experiment were analytical reagents and used without further purification. Deionized water was used in all synthesis and treatment processes. Tetrabutyl titanate (TBOT, C₁₆H₃₆O₄Ti), melamine (C₃H₆N₆), anhydrous ethanol (C₂H₆O) and tertiary butyl alcohol (TBA, C₄H₁₀O) were purchased from Sinopharm Chemical Reagent Co., Ltd. Ethylenediamine tetraacetic Acid (Na₂-EDTA, C₁₀H₁₈N₂Na₂O₁₀) and p-benzoquinone (*p*-BQ, C₆H₄O₂) were purchased from Aladdin Industrial Corporation.

2.2. Sample preparation

Macro/mesoporous g-C₃N₄/TiO₂ heterojunction photocatalysts were fabricated by calcining the mixtures of the melamine and amorphous macro/mesoporous TiO₂ powders. First, the amorphous macro/mesoporous TiO₂ powders were prepared according to the literature procedure [44]. In brief, 20 mL of TBOT was added dropwise dissolved in 200 mL of distilled water without vigorous stirring. The mixture of the reagents was aged at room temperature for 36 h. Subsequently, the white precipitates were collected by filtration rinsed four times with distilled water and anhydrous ethanol alternately. After the washed samples were dried in an oven 60 °C for 12 h, the amorphous macro/mesoporous TiO₂ powders

were obtained. Second, 3 g of melamine was dispersed in 100 mL hot distilled water, and then 0.5 g of amorphous macro/mesoporous TiO₂ was added. The suspension solution were transferred to a 250 mL beaker and then dried in an oven at 100 °C for 12 h. Subsequently, this dried mixture was placed in an alumina crucible with a cover and then calcined in a muffle furnace for 2 h at 550 °C with a ramping rate of 5 °C min⁻¹ in air atmosphere. After cooling down to room temperature, the final light yellow macro/mesoporous g-C₃N₄/TiO₂ products were obtained. In order to discuss the role of g-C₃N₄ content on the photocatalytic activity of g-C₃N₄/TiO₂ heterojunction photocatalysts, samples with different amount of melamine in the precursors were prepared under the same conditions. The products were named as CNTx, where the x referred to the mass weight of melamine used (Table 1). For example, CNT3 represented the sample prepared from 3 g of melamine and 0.5 g of amorphous macro/mesoporous TiO₂. For comparison, pure g-C₃N₄ and TiO₂ (CNT0) were directly annealed at the above condition by using melamine and amorphous macro/mesoporous TiO₂ as feedstocks, respectively.

2.3. Sample characterization

The powder X-ray diffraction (XRD) patterns were acquired on Bruker D8 Advance X-ray diffractometer (Bruker AXS, German) with Cu K α 1 radiation ($\lambda = 1.5418 \text{ \AA}$) at a scanning speed of 0.02° s⁻¹. The accelerating voltage and applied current were 40 KV and 20 mA, respectively. The morphology of the g-C₃N₄/TiO₂ powders was observed on a field emission scanning electron microscope (FESEM) (JSM-7000F, Japan) with an acceleration voltage of 15 kV and a transmission electron microscope (TEM) (Tecnai G20, USA) using an acceleration voltage of 200 kV, respectively. Fourier transform infrared (FT-IR) spectra were conducted on Nicolet 5700 FT-IR spectrometer with the samples dispersed in KBr desiccative in the range of 400–4000 cm⁻¹. TGA-7 analyzer (PE, USA) was used to characterize the thermal chemical and physical properties of the samples. Nitrogen adsorption-desorption isotherms were analyzed by a Micromeritics ASAP 2020HD 88 nitrogen adsorption apparatus (USA). The samples were degassed at 180 °C for 4 h prior to nitrogen adsorption measurements. The S_{BET} of the samples were measured by adsorption segments in the relative pressure P/P₀ range of 0.05–0.20. The data of desorption were used for determining the pore size using the Barrett-Joyner-Halenda (BJH) method. X-ray photoelectron spectroscopy (XPS) was measured on a K-Alpha (1486.68 eV) X-ray sources (USA). The RhB concentration in aqueous solution was determined at 552 nm by a UV-vis spectrophotometer (UV-2550, Shimadzu, Japan). The UV-vis absorption spectra of as-prepared photocatalysts were measured by a Shimadzu UV-vis spectrophotometer (Japan) with BaSO₄ used as a reflectance standard. PL spectra of the samples were measured by a PerkinElmer LS55 fluorescence spectrophotometer (Germany, slit 10 nm, scanning speed 1200 nm min⁻¹, excitation wavelength 320 nm). The total organic carbon (TOC) tests were performed by the Apollo9000 TOC analyzer before and after photocatalytic reaction for 80 min.

2.4. Measurement of photocatalytic activity

The photocatalytic activity of the photocatalysts was estimated by photocatalytic decomposition of RhB aqueous solution at room temperature under visible light irradiation. Detail experiments were examined as follows: 0.04 g of the sample was dispersed in 20 mL of deionized water. The resulting suspensions were sonicated for 40 min and then poured into a dish with diameter of about 9 cm, which was dried in an oven at 60 °C for 3 h to evaporate the water. Secondly, 30 mL of RhB (1 × 10⁻⁵ M) solution was transferred into the above dish with the sample. Prior to visible-

Table 1

Effects of content of melamine in the precursors on physical properties of as-prepared samples.

Sample	S_{BET} ($\text{m}^2 \text{ g}^{-1}$)	Pore size (nm)	PV^{a} ($\text{cm}^3 \text{ g}^{-1}$)	ACS^{b} (nm)	$\text{g-C}_3\text{N}_4^{\text{c}}$ content (%)	E_g (eV)
TiO ₂	34.8	21.7	0.189	28.4 (A)	0	3.24
CNT-1	40.9	8.0	0.0816	24.7 (A)	7.8	3.20
CNT-2	64.4	12.4	0.199	16.1 (A)	17.2	2.84
CNT-3	70.2	11.0	0.193	10.5 (A)	28.3	2.83
CNT-4	39.2	16.1	0.158	8.4 (A)	37.5	2.82
$\text{g-C}_3\text{N}_4$	14.3	27.5	0.0986	—	100	2.80

^a PV: pore volume.

^b ACS: average crystallite size. A for anatase.

^c $\text{g-C}_3\text{N}_4$ content was determined by TGA analysis under air atmosphere.

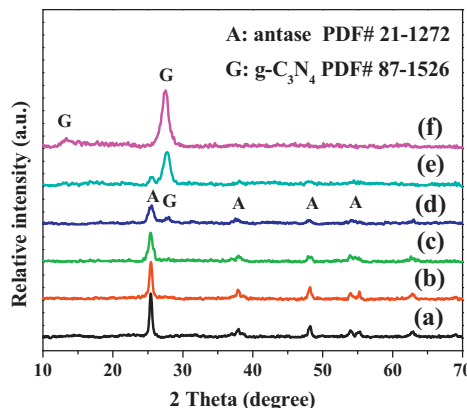


Fig. 1. X-ray diffraction patterns of various photocatalysts: (a) CNT0 (pure TiO₂), (b) CNT1, (c) CNT2, (d) CNT3, (e) CNT4 and (f) $\text{g-C}_3\text{N}_4$.

light illumination, the suspensions of catalysts and RhB were kept in the dark for 2 h to reach an adsorption-desorption equilibrium. A 350 W xenon arc lamp equipped with a UV-cut off filter (420 nm) served as a visible-light source to inspire photocatalytic process. After visible light illumination for every 20 min, the RhB solution was collected to measure the concentration change of the RhB solution at 552 nm by UV-vis spectrophotometer. As for RhB solution with a low concentration, the photocatalytic decolorization process is a pseudo-first-order reaction: $\ln(C_0/C_t) = kt$, where the k is the apparent rate constant, C_0 and C_t represent the concentration of RhB at initial stage and after irradiated for some time, respectively.

3. Results and discussion

3.1. XRD pattern

XRD analysis was used to determine the phase structures and crystal size of the as-prepared samples. The XRD patterns of the pure TiO₂ (CNT0), $\text{g-C}_3\text{N}_4$ and CNTx heterojunction photocatalysts are shown in Fig. 1. It can be seen from Fig. 1a that the peak at 25.4° (101), 37.7° (004), 48.2° (200) and 54.1° (105) clearly indicated the formation of anatase phase (JCPDS No. 21-1272). For the pure $\text{g-C}_3\text{N}_4$, the characteristic diffraction peaks at 13.1° and 27.4° were corresponding to the (100) and (002) plane diffraction of $\text{g-C}_3\text{N}_4$ (JCPDS No. 87-1526). For the CNT1 and CNT2 samples, no characteristic diffraction peaks of $\text{g-C}_3\text{N}_4$ were found. This may be ascribed to the fact that the two samples have a lower $\text{g-C}_3\text{N}_4$ content and poorer crystallization [45,46]. However, it was evident that the characteristic diffraction peaks of both anatase and $\text{g-C}_3\text{N}_4$ were observed in the CNT3 and CNT4 heterojunction photocatalysts. Further observation showed that with increasing the content of melamine in the precursors, the diffraction peaks intensity of $\text{g-C}_3\text{N}_4$ became stronger. In contrast, the diffraction peaks intensity of anatase became weaker. This is because the content of $\text{g-C}_3\text{N}_4$ in both CNT3 and CNT4 samples gradually increased [39].

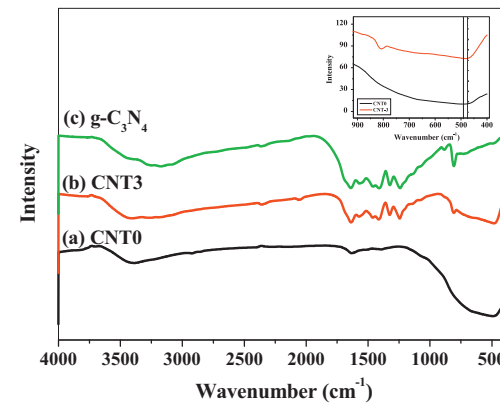


Fig. 2. FT-IR spectra of various photocatalysts: (a) CNT0 (pure TiO₂), (b) CNT3, (c) $\text{g-C}_3\text{N}_4$. Inset is the enlarged plots of FT-IR of CNT0 and CNT3.

The average crystal size of anatase was estimated from the main diffraction peaks of anatase (101) by using Scherrer's equation [40], and the corresponding results are listed in Table 1. The anatase (101) average crystallite size of CNTx samples gradually decreases from 28.4 nm to 8.4 nm with increasing the content of melamine in the precursors. This may be ascribed to fact that melamine suppressed the crystallite growth of the anatase TiO₂. In addition, there is no obvious shift in the peak positions for all CNTx heterojunction photocatalysts, suggesting that $\text{g-C}_3\text{N}_4$ was probably deposited on the surface of anatase instead of being incorporated into the lattice of anatase particles [47].

3.2. FTIR spectroscopy analysis

The FTIR spectroscopy was used to identify the composition information and chemical bonding of pure TiO₂, $\text{g-C}_3\text{N}_4$ and CNTx heterojunction photocatalysts, as shown in Fig. 2. For the pure TiO₂ (CNT0), the main peaks at 400–700 cm⁻¹ were assigned to Ti–O–Ti and Ti–O stretching vibration modes in anatase crystals. Another two wide peaks at 1650 and 3400–3500 cm⁻¹ were corresponding to hydroxyl group and physically adsorbed water, respectively [40,46]. In the FTIR spectrum of $\text{g-C}_3\text{N}_4$, the absorption peaks ranging from 1200 to 1640 cm⁻¹ confirmed the presence of two main bonds in the products. The peak at 1638 cm⁻¹ corresponded to the $\text{sp}^2 \text{C}=\text{N}$ stretching vibration modes, while the peaks at 1242 cm⁻¹, 1324 cm⁻¹ and 1411 cm⁻¹ were assigned to the aromatic $\text{sp}^3 \text{C}=\text{N}$ bonds. In addition, the peak at 807 cm⁻¹ was due to the out-of-plane skeletal bending modes of triazine [33,45]. For the CNT3 sample, it can be clearly observed that the main characteristic peaks of TiO₂ and $\text{g-C}_3\text{N}_4$ appeared. It is worth mentioning that compared with the main characteristic peak of Ti–O–Ti stretching vibration for pure TiO₂ (peak at 490 cm⁻¹), the slight shift to a lower wavenumber in CNT3 (peak at 483 cm⁻¹) was observed (the inset in Fig. 2), which confirmed the formation of the close interfacial contact between $\text{g-C}_3\text{N}_4$ and TiO₂ [43]. The heterojunction struc-

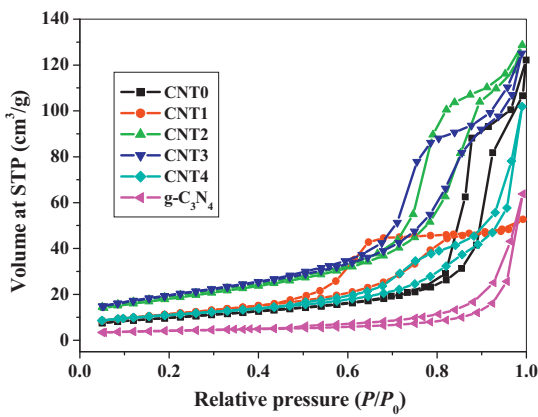


Fig. 3. N_2 adsorption-desorption isotherms of $\text{g-C}_3\text{N}_4$ and CNT_x heterojunction photocatalysts.

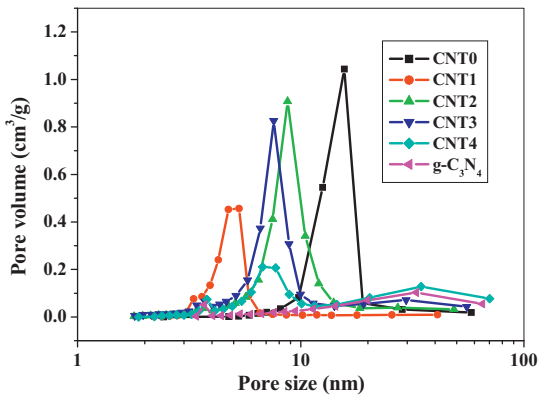


Fig. 4. The corresponding pore size distribution curves of $\text{g-C}_3\text{N}_4$ and CNT_x heterojunction photocatalysts.

ture is in favor of the separation of photoelectrons and holes and promotes a synergetic effect to improve the photocatalytic activity [24,41], which will be discussed in detail in the following sections.

3.3. Nitrogen adsorption

Commonly, higher specific surface areas (S_{BET}) and larger pore volumes of photocatalysts were contributed to an enhanced photocatalytic activity owing to the presence of a large amount of surface active sites, so it can absorb and transfer reactant molecules easily via the interconnected porous structure, and increase the photocatalytic performance [48]. The effect of melamine content in the precursors on the BET surface areas pore parameters of CNT_x heterojunction photocatalysts were investigated using the nitrogen adsorption instrument. The nitrogen adsorption-desorption isotherms and the pore size distributions curves of pure TiO_2 , $\text{g-C}_3\text{N}_4$ and CNT_x heterojunction photocatalyst are showed in Figs. 3 and 4, respectively. It can be seen from Fig. 3 that all samples have the adsorption-desorption isotherms of type IV according to the IUPAC classification, indicating the existence of mesopores [43,45–47,49]. The isotherms of $\text{CNT}0$ and CNT_x heterojunction photocatalysts have two hysteresis loops, indicating bimodal pore size distributions in the mesoporous (2–50 nm) and macroporous (>50 nm) region. At low P/P_0 range from 0.5 to 0.8, the shape of the hysteresis loop is of Type H2, indicating the existence of ink-bottle pores with broad bodies and narrow necks, which are related to the interconnected pore structure [50]. At high P/P_0 range from 0.8 to 1.0, the shape of the hysteresis loop is of Type H3, indicating the presence of slit-shaped pores resulted from aggregation of

plate-like particles. The isotherms show high absorption at a high P/P_0 range (approaching 1.0), implying the formation of large mesopores and macropores, which can be confirmed from SEM results (Fig. 5) [45,51]. Further observation shows that the isotherms of the CNT_x samples shift up compared to pure TiO_2 ($\text{CNT}0$) and $\text{g-C}_3\text{N}_4$ samples, indicating the CNT_x samples with higher surface areas and pore volumes [47].

The pore distributions of the all samples (except pure $\text{g-C}_3\text{N}_4$) were very broad in Fig. 4, further demonstrating the presence of larger mesopores and macropores. The BET surface area, pore size and pore volume of all photocatalysts are presented in Table 1. The CNT_x samples exhibited an increase in specific surface areas compared with pure $\text{g-C}_3\text{N}_4$ and TiO_2 ($\text{CNT}0$). Especially, the specific surface areas and pore volumes of CNT_x nanocomposites gradually increased with increasing of melamine content in the precursors (from 1 to 3 g). The reason is that $\text{g-C}_3\text{N}_4$ has low density and smaller particle size [45]. Nevertheless, further increasing the melamine content (from 3 to 4 g) resulted in the decrease in the surface areas and pore volumes. This is ascribed to the fact that excess $\text{g-C}_3\text{N}_4$ in the hybridization process tended to self-aggregation, thereby leading to the decrease in specific surface areas and pore volumes [46].

3.4. SEM and TEM analysis

The external morphologies and the microstructures information of the CNT_x heterojunction photocatalysts were studied by using SEM and TEM. As shown in Fig. 5a, the as-prepared pure TiO_2 ($\text{CNT}0$) exhibited a relatively regular macroporous structure with pore sizes ranging from 1.0 μm to 2.50 μm and the thicknesses of the walls ranging from 0.5 μm to 0.8 μm . Further observation showed that the ultralong macroscopic channels of 50 μm in length dimension were arranged parallel to each other and orthogonal to one side of the monolithic particles (Fig. 5b). Moreover, the walls of the macroporous TiO_2 were composed of small interconnected TiO_2 particles with sizes from 200 to 400 nm, which is similar with the previous results reported by Yu et al [1,44]. It is speculated that the continuous open-ended tube-like macroporous channels may act as efficient light-transport pathways for introducing gas molecules and photoenergy into the interior space of TiO_2 [1]. The $\text{CNT}3$ sample preserved a macroscopic network structure with a relatively regular array of macropores, as shown in Fig. 5c–e. The sizes of the macropores were similar to those of the pure TiO_2 sample. It was interesting to note that some macropores of the $\text{CNT}3$ sample were filled with $\text{g-C}_3\text{N}_4$. The $\text{g-C}_3\text{N}_4$ particles were dispersed and highly embedded within the TiO_2 macroporous system or loaded on the surface TiO_2 pore walls. These highly integrated composite systems made the $\text{CNT}3$ sample have a high surface area, which was in good agreement with BET results. The morphological and structural feature of $\text{CNT}3$ heterojunction was further investigated by TEM and HRTEM, as shown in Fig. 5f and g, respectively. The TEM image of the $\text{CNT}3$ sample revealed a small amount of TiO_2 particles with sizes ranging from ca. 25 to 35 nm were deposited on the surface of $\text{g-C}_3\text{N}_4$, which were in excellent agreement with the sizes of anatase TiO_2 determined from the corresponding XRD results (see Table 1). The lattice fringes can be clearly observed in Fig. 5g, implying the $\text{CNT}3$ sample with good crystallinity of anatase TiO_2 , and the lattice spacing of ca. 0.35 nm can be ascribed to the (101) plane of TiO_2 . Based on SEM, TEM and HRTEM analyses, it can be inferred that the $\text{g-C}_3\text{N}_4$ particles were successfully embedded into the TiO_2 macroporous framework, suggesting the formation of heterojunction between $\text{g-C}_3\text{N}_4$ and TiO_2 in the $\text{CNT}3$ nanocomposite [16]. The close interfacial contact may be of significance to transfer photoinduced carriers from $\text{g-C}_3\text{N}_4$ to TiO_2 surface. Therefore, it was

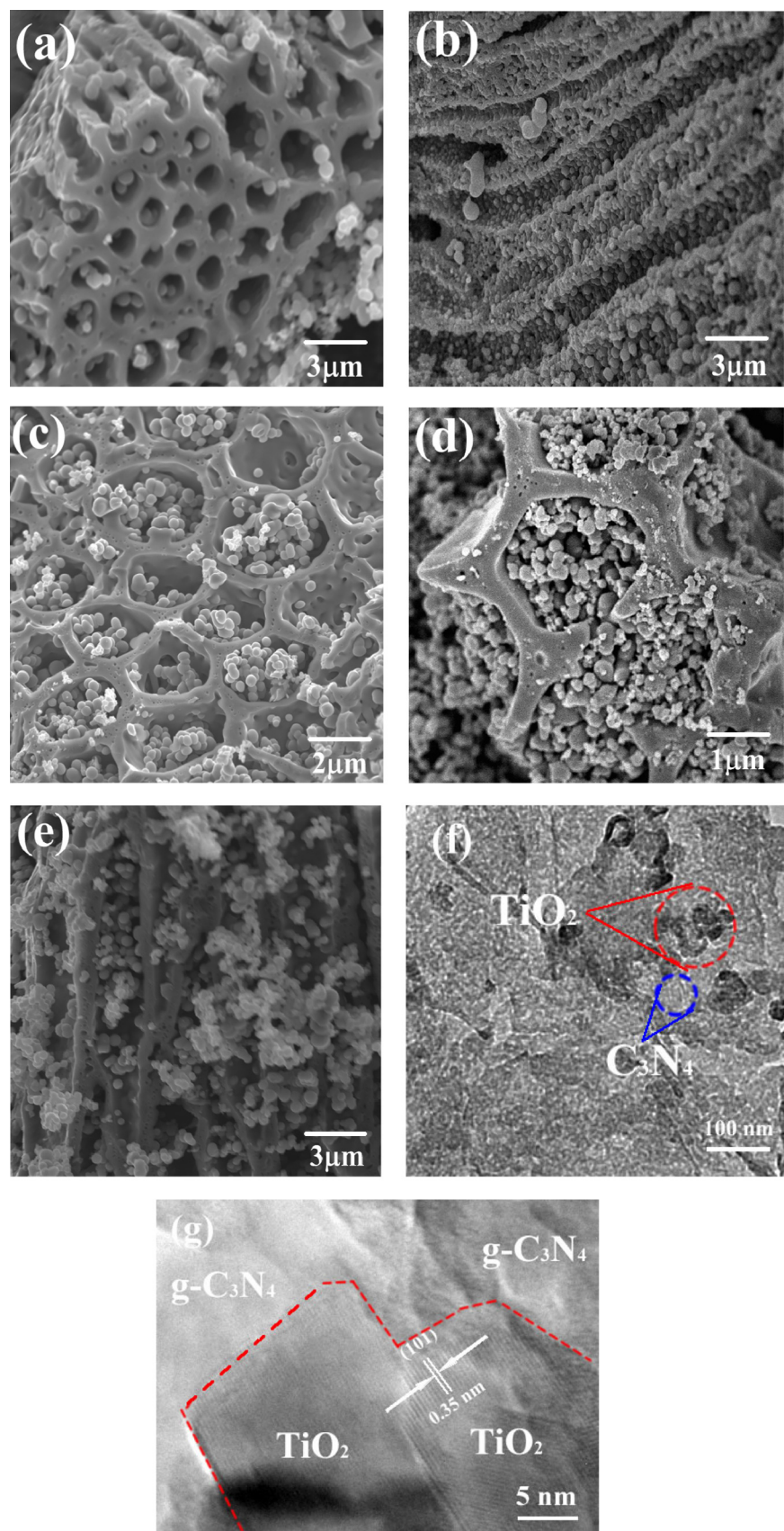


Fig. 5. SEM images of various photocatalysts: (a) (b) CNT0 (pure TiO_2) and (c) (d) (e) CNT3, TEM (f) and HRTEM (g) images of CNT3 heterojunction photocatalyst.

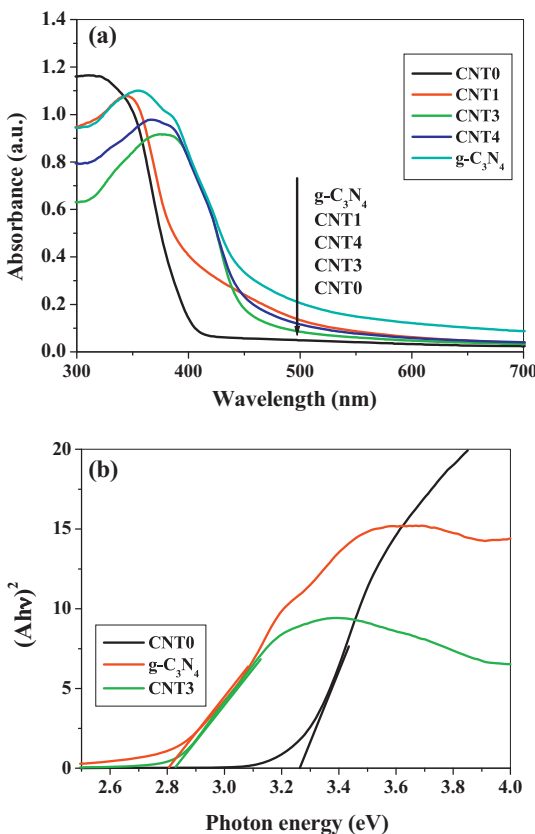


Fig. 6. Optical property of as-prepared photocatalysts. (a) UV-vis diffuse reflectance spectra of the g-C₃N₄ and CNTx heterojunction photocatalyst. (b) The band gap of CNT0 (pure TiO₂), g-C₃N₄ and CNT3 samples determined from the (αhv)² versus photon-energy.

reasonable that an enhanced visible light photocatalytic activity was expected for the CNTx composites.

3.5. UV-vis diffuse reflection spectra

In general, the optical absorption properties of photocatalyst play an important role in determining the photocatalytic performance, especially for photodegradation of organic contaminants under visible light irradiation. To study the light absorption abilities of pure g-C₃N₄, TiO₂ nanoparticles and the CNTx composites, we investigated the UV-vis diffuse reflectance spectra (DRS), as shown in Fig. 6a. For pure TiO₂ (CNT0), the absorption wavelength was under 390 nm, consistent with the intrinsic band gap of anatase TiO₂ (about 3.24 eV). This implied that the pure TiO₂ could only have a response to UV light [47,52]. However, g-C₃N₄ exhibited a wider photoabsorption from ultraviolet to visible light, and its band gap absorption edge was around 450 nm (the band gap 2.80 eV), which resulted from the charge-transfer response from valence band (VB) migrated by N 2p orbit to the conduction band (CB) formed by C 2p orbit [35,53]. It is notable that the CNTx composites displayed the broader absorption edge and extended to the visible region as compared to that of pure TiO₂. This may be ascribed to the presence of g-C₃N₄ on TiO₂ surface. Further observation showed that with increasing the melamine content in the precursors, there was a red shift of the UV-vis absorption edge for all CNTx composites, indicating the decrease in the band gap [54]. The bandgap of photocatalysts were calculated by using the following Kubelka-Munk function Eq. (1):

$$(\alpha h\nu)^2 = A(h\nu - E_g) \quad (1)$$

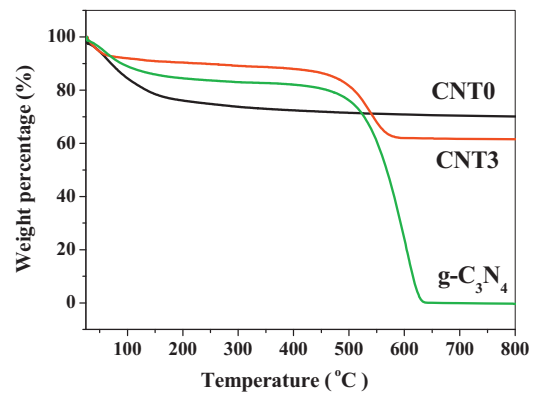


Fig. 7. TGA curves of the CNT0 (pure TiO₂), g-C₃N₄ and CNT3 heterojunction photocatalyst.

Table 2

The χ, E_{CB}, E_{VB} and E_g for TiO₂ and g-C₃N₄ at the point of zero charge.

Sample	χ (eV)	E _{CB} (eV)	E _{VB} (eV)	E _g (eV)
TiO ₂	5.81	-0.31	2.93	3.24
g-C ₃ N ₄	4.73	-1.17	1.63	2.80

χ, E_{CB}, E_{VB} and E_g denote absolute electronegativity, calculated CB edge, calculated VB position and band gap energy, respectively.

where α, hν, E_g and A were absorption coefficient, the photon energy, direct bandgap and a constant, respectively. The plot of (αhv)² versus hν is shown in Fig. 6b, the band gap energies of various photocatalysts are shown in Table 1. These results exhibited that the band gaps of CNTx heterojunction photocatalysts gradually became narrower with increasing the content of melamine in precursors.

3.6. TGA analysis

The amount of g-C₃N₄ in the final products was determined by TGA analysis under air atmosphere from room temperature to 800 °C at a heating rate of 10 °C min⁻¹. Fig. 7 presents the comparison of TGA curves of pure TiO₂ (CNT0), g-C₃N₄ and CNT3 samples. For CNT0, there was a very low weight loss from 25 °C to 300 °C, which could be ascribed to the loss of surface absorbed water. However, the pure g-C₃N₄ exhibited two weight loss regions in the TGA curves. The former weight loss occurred at around 25–300 °C due to desorption of surface bound water. The later weight loss from 300 °C to 650 °C was due to the combustion of g-C₃N₄ in the air atmosphere. It can be seen that the CNT3 sample also had two similar weight loss regions and the content of the g-C₃N₄ could be estimated from the later weight loss region (300–650 °C) [45]. Therefore, the actual amount of g-C₃N₄ in the CNT3 sample was about 28.3%. The corresponding amount of g-C₃N₄ on the CNT1, CNT2, and CNT4 samples were estimated by the above method to be about 7.8, 17.2 and 37.5 wt%, respectively (Table 2).

3.7. XPS analysis

The surface chemical compositions of CNT3, pure TiO₂ and g-C₃N₄ samples were further investigated by X-ray photoelectron spectroscopy (XPS). It was clearly seen from Fig. 8a that all signals of Ti, O, N, and C were found in the survey XPS spectrum of the CNT3 sample. In addition, no peaks of other elements were detected, implying that CNT3 heterojunction photocatalyst is mainly composed of Ti, O, N, and C elements. However, only signals of N, O and C were found in pure g-C₃N₄ sample, and the peak of O 1s was ascribed to the adsorbed hydroxyl groups [55]. For pure TiO₂, the

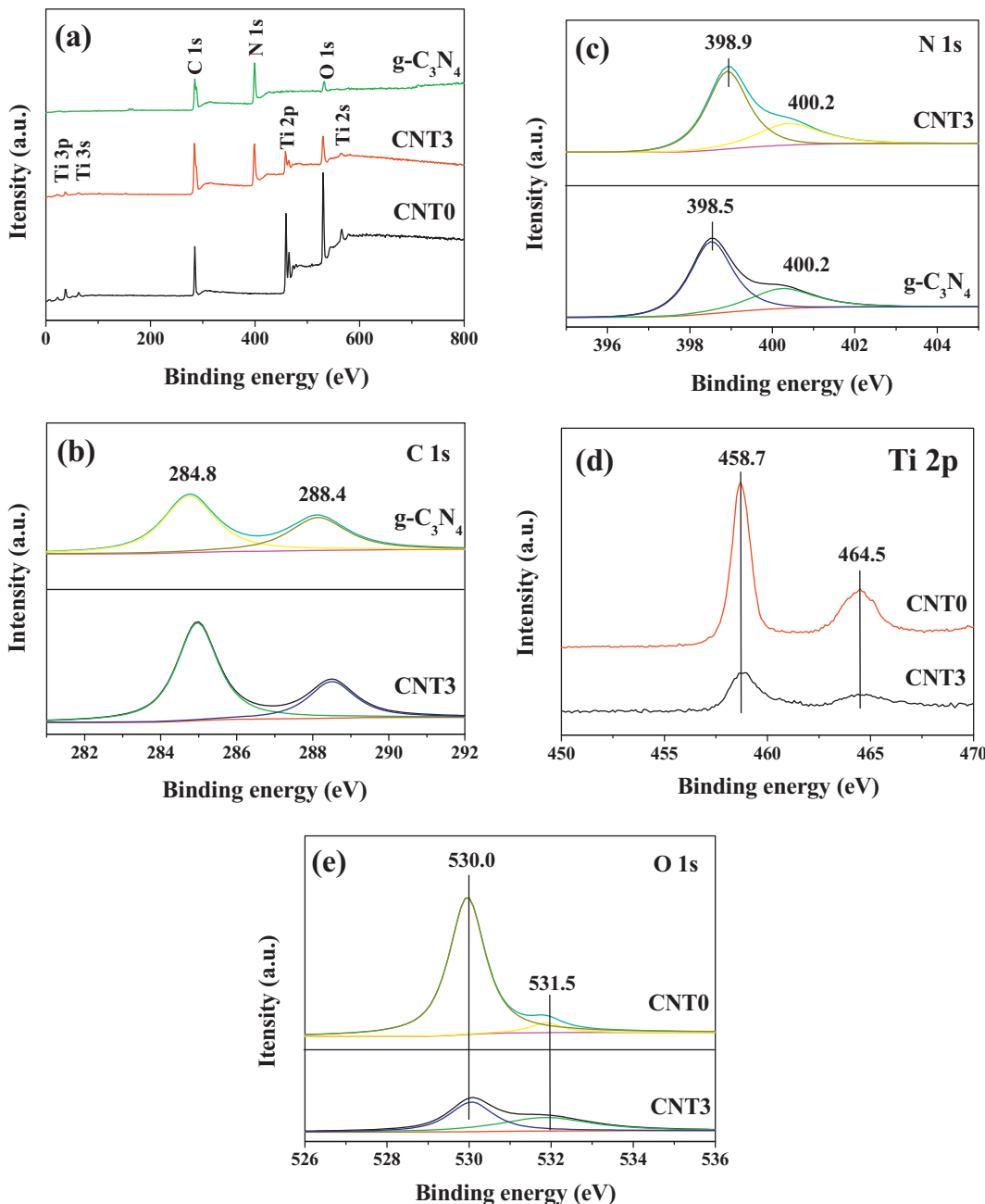


Fig. 8. XPS survey spectra of CNT3, g-C₃N₄ and CTO (pure TiO₂) (a), high resolution C 1s spectra of CNT3 and g-C₃N₄ (b), high resolution N 1s spectra of CNT3 and g-C₃N₄ (c), high resolution Ti 2p spectra of CNT3 and CTO (pure TiO₂) (d) and high resolution spectra O 1s of CNT3 and CTO (pure TiO₂) (e).

peaks of Ti, O and C appeared, and the carbon peak was attributed to the residual carbon from adventitious hydrocarbon from XPS instrument itself.

Fig. 8b presents the corresponding high-resolution C1s spectra of the CNT3 and pure g-C₃N₄. It can be seen that both the samples have the two C1s peaks at binding energies of 284.8 and 288.4 eV. The former was strong and corresponding to the C–C coordination of the surface adventitious carbon species from the XPS instrument itself, whereas the later one was ascribed to sp³-bonded carbon in C–N of g-C₃N₄ [48]. Fig. 8c shows the high-resolution N 1s spectrum of the CNT3 sample in comparison with that of pure g-C₃N₄. It can be clearly observed from the high-resolution N 1s XPS spectra that there were asymmetrical and broad features in both samples due to the co-existence distinguishable nitrogen models. The N 1s peak could be divided into two peaks located at binding energies

of ca. 398 and 400 eV, which were assigned to sp²-hybridized pyridine nitrogen (C=N–C) and tertiary nitrogen (N–C₃), respectively [45]. It was notable that the binding energy of pyridine nitrogen in the CNT3 sample (398.9 eV) increased 0.4 eV when compared with that of pure g-C₃N₄ (398.5 eV), also confirming the interfacial interaction between g-C₃N₄ and TiO₂ in the CNT3 composite. Fig. 8d presents the high resolution Ti 2p spectra of the CNT3 and pure TiO₂. The two deconvolution peaks at binding energies of 458.7 and 464.5 eV were observed in both samples, which corresponded to the Ti 2p_{3/2} and Ti 2p_{1/2} of TiO₂, respectively [20]. Fig. 8e depicts the O 1s high-resolution spectra of CNT3 and pure TiO₂ and the two peaks located at binding energies of at 530.0 and 531.5 eV were ascribed to the Ti-O band and surface –OH groups, respectively [39]. It is notable that no obvious characteristic peaks for Ti-C (N) could be observed, further indicating that the N and C elements do

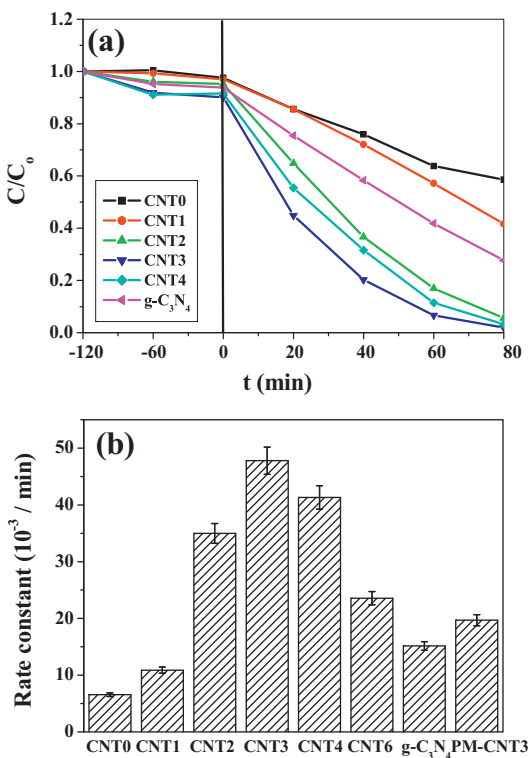


Fig. 9. (a) Photocatalytic activity curves of g-C₃N₄ and CNTx photocatalysts for the degradation of RhB aqueous solution under visible light irradiation. (b) Comparison of the apparent rate constants k (10^{-3} min⁻¹) of the g-C₃N₄, CNTx and PM-CNT3 samples of the degradation of RhB under visible light irradiation.

not enter into the lattice of the TiO₂, which was in accordance with the above XRD, FT-IR, TEM and UV-vis results.

3.8. Photocatalytic activity

Rhodamine B (RhB), methyl orange (MO) and other organic dyes are widely used in industrial processes, such as cosmetics, textile, printing and photographic industries. A considerable fraction of dyes is lost in the dying process and released into the water streams, which has various harmful influences on human healthy by causing eye or skin irritation, or gastrointestinal irritation by inhalation, and causes a series of serious environmental problems. Therefore, it is necessary to degrade organic dyes in industrial waste water. Control experiments demonstrated that the concentration of Rhodamine B (RhB) was unchanged in the absence of either irradiation or photocatalyst, implying that RhB was considerably stable and the degradation by itself was negligible. Fig. 9a presents a comparison of RhB concentration changes in the presence of g-C₃N₄/TiO₂ heterojunction photocatalysts prepared at different loading of melamine in the precursors. As we can see from Fig. 9a, the degradation rates of RhB were slow over separate pure TiO₂ (CNT0) and g-C₃N₄ catalysts. Interestingly, the g-C₃N₄/TiO₂ heterojunction photocatalysts exhibited significantly enhanced activity in comparison with pure g-C₃N₄ and TiO₂ nanoparticles. Further observation indicated that the photocatalytic activity of the g-C₃N₄/TiO₂ composites highly depended on the amount of incorporated g-C₃N₄. Fig. 9b displays a comparison of apparent reaction rate constant (k) of pure TiO₂ (CNT0), CNT1, CNT2, CNT3, CNT4, CNT6, pure g-C₃N₄ and PM-CNT3 samples for photocatalytic degradation of RhB at room temperature in air. For pure TiO₂ (CNT0), its k was 6.57×10^{-3} min⁻¹, indicating that TiO₂ had a weak photocatalytic activity due to its limited light adsorption ability under visible light region (Fig. 9b).

For the CNT1, CNT2 and CNT3 samples, the photocatalytic performance significantly increased. In particular, when the content of the melamine in precursors was controlled to be 3 g (CNT3 sample), the k reached a highest value of 47.8×10^{-3} min⁻¹, exceeding that of pure TiO₂ (6.6×10^{-3} min⁻¹) and g-C₃N₄ (15.2×10^{-3} min⁻¹) by factor of 7.2 and 3.1, respectively. With further increase of the melamine content to 4 g in the precursors, although the photocatalytic preformance of the CNT4 had a slight decrease with a rate constant of 41.3×10^{-3} min⁻¹, it still possessed a higher photocatalytic activity than CNT0 and g-C₃N₄. In general, integrating TiO₂ with g-C₃N₄ to form heterostructure is an efficient and feasible route to enhance the photocatalytic activity of TiO₂. However, further experimental results indicated that the CNT6 sample had an obviously decreased photocatalytic preformance (23.6×10^{-3} min⁻¹) when the melamine content was 6 g in the precursors. Why did the as-prepared CNT3 sample exhibit the highest photocatalytic activity? Firstly, the photodecomposition activity of photocatalysts is strongly dependent on the band gap of the photocatalysts and the wavelength of light used for excitation. CNT3 sample had a narrower band gap of 2.83 eV compared with TiO₂ of 3.24 eV. This implied that CNT3 sample was more active than CNT0 to excite more photogenerated electrons and holes under visible light irradiation. Secondly, CNT3 sample possessed a highest surface area of $70.2 \text{ m}^2 \text{ g}^{-1}$, which would offer more active sites and be beneficial for the decomposition of RhB. Thirdly, it was most crucial that an excellent heterostructure between TiO₂ and g-C₃N₄ was formed in the CNT3 sample, which significantly restrained the recombination of the photogenerated electrons and holes, thereby improving efficiently the photocatalytic activity of the CNT3 sample. Moreover, g-C₃N₄ content in the precursors also played an important role in constructing effective heterointerfaces in g-C₃N₄/TiO₂ composites, as reported in literature [45]. More g-C₃N₄/TiO₂ heterojunction interfaces would be formed in g-C₃N₄/TiO₂ composite with the suitable g-C₃N₄ content, which facilitated the separation of photogenerated hole-electron pairs, resulting in the strengthened photocatalytic activity. However, when g-C₃N₄ content exceeded a certain value, the quantities and quality of effective heterointerfaces would decrease in g-C₃N₄/TiO₂ composites [56]. It was not beneficial for the charge transfer at heterointerfaces, which as a consequence would decrease the photocatalytic ability.

Fig. 10 shows the changes in the optical absorption spectra of the RhB aqueous solution over the CNT3 sample with visible light irradiation time. As the irradiation time was prolonged, the intensities of adsorption peak at 554 nm drops gradually. Furthermore, RhB dye was degraded completely by the CNT3 photocatalyst after 80 min under visible light irradiation.

It is essential for RhB in water solution to be completely mineralized by photocatalysts. However, it is not easy to achieve higher mineralization efficiency during the photocatalysis process, especially under visible light irradiation. In general, the ethyl groups of RhB were first removed, and the cycloreversion subsequently occurred during the degradation of RhB. After that, it was gradually decomposed into other intermediate organic products, CO₂ and H₂O [57]. The total organic carbon (TOC) analysis of RhB solutions before and after photocatalytic reaction for 80 min was performed by TOC analyzer and the corresponding removal efficiency is shown in Fig. 10b. It can be observed that the decay of TOC was 16.1%, 19.3%, 45.6%, 52.4%, 47.0%, 39.1%, 34.6% and 36.8% for CNT0, CNT1, CNT2, CNT3, CNT4, CNT6, g-C₃N₄ and PM-CNT3 composite respectively. These experiment results were in accordance with the above the photocatalytic activity of various catalysts (see Fig. 9b).

To further prove the close relation between the improved photocatalytic activity and the presence of heterointerfaces of g-C₃N₄ and TiO₂ in nanocomposites, a mechanically blended g-C₃N₄ and TiO₂ sample (denoted as PM-CNT3) was also prepared. The amount

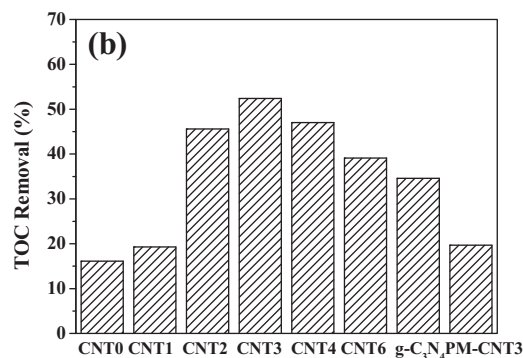
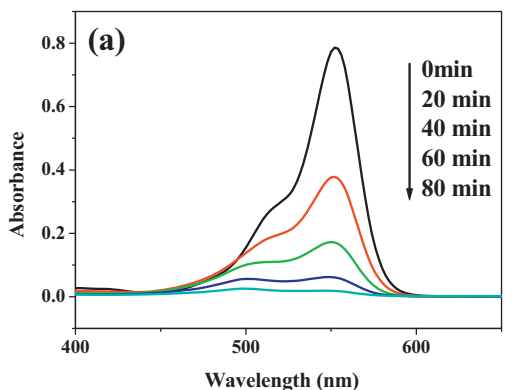


Fig. 10. The adsorption peak changes of RhB aqueous solution in the presence of CNT3 heterojunction photocatalyst with increasing of irradiation time under visible light ($\lambda > 420$ nm) (a) and the TOC removal of RhB in the presence of various catalysts under visible light irradiation for 80 min (b).

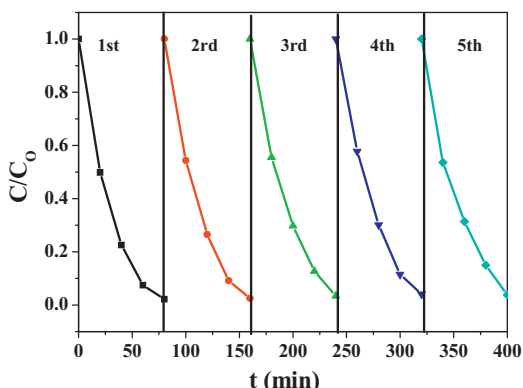


Fig. 11. Circulating runs in the decomposition of RhB for CNT3 heterojunction photocatalyst under visible-light irradiation.

of $\text{g-C}_3\text{N}_4$ and TiO_2 in the PM-CNT3 sample was the same as that in the CNT3 composite. It can be clearly seen from Fig. 9b that the apparent rate constant of PM-CNT3 sample obviously decreased (only up to $19.7 \times 10^{-3} \text{ min}^{-1}$) compared to that of CNT3. These results confirmed that the formation of heterojunction structure between $\text{g-C}_3\text{N}_4$ and TiO_2 in the hybrids was the most crucial factor to strengthen the high photocatalytic performance of the resulting nanocomposite samples [58].

In consideration of the practical applications, it is essential to evaluate the stability of the as-prepared samples during photocatalytic reaction. The recycling experiments were performed for the photocomposition of RhB over the CNT3 sample under visible light irradiation. As can be seen from Fig. 11, the photocatalytic activity of the CNT3 sample did not show a significant decrease after five recycles, indicative of the excellent stability of the CNT3

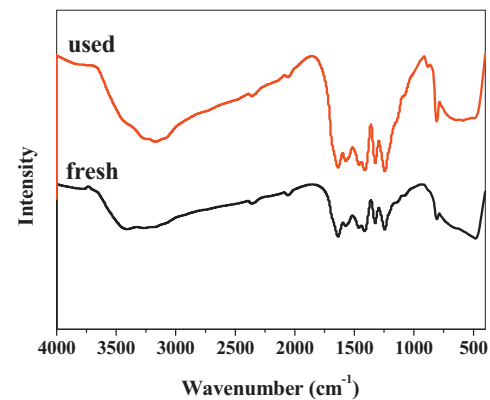


Fig. 12. FT-IR patterns of the CNT3 heterojunction photocatalyst before and after 5 circulating runs.

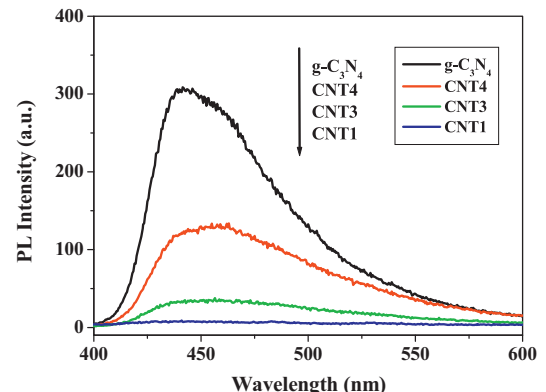


Fig. 13. PL spectra of $\text{g-C}_3\text{N}_4$ and CNT_x ($x = 1, 3$ and 4) photocatalysts under 320 nm excitation.

photocatalyst. FT-IR patterns were used to further investigate the chemical stability of the CNT3 sample. Fig. 12 clearly shows that FT-IR patterns of the reused CNT3 had not changed significantly compared with those of as-prepared CNT3 catalyst. This suggested that chemical structures of the CNT3 catalyst were stable during the photocatalytic reactions.

3.9. Photoluminescence (PL) analysis

It is well known that photoluminescence (PL) analysis is a very useful technique to disclose the migration, transfer and separation efficiency of the photoexcited charge carriers in a photocatalytic material because PL emission of photocatalyst mainly results from the charge carrier recombination [59]. Usually, the lower the PL intensity is, the better the separation efficiency of photoinduced electron-hole pairs would be, and thus the higher the photocatalytic performance would be. Fig. 13 presents the PL spectra of the pure C_3N_4 and $\text{g-C}_3\text{N}_4/\text{TiO}_2$ composites under the excitation wavelength of 320 nm at room temperature. In the case of the pure $\text{g-C}_3\text{N}_4$, the strong peak centered at about 442 nm was ascribed to the band-band PL phenomenon with the energy of light corresponding to the band gap of $\text{g-C}_3\text{N}_4$ (2.80 eV) [43]. Though the PL spectra of the $\text{g-C}_3\text{N}_4/\text{TiO}_2$ composites were similar to that of pure $\text{g-C}_3\text{N}_4$, the emission peak intensities decreased sharply. Besides, the significant PL quenching was observed in the $\text{g-C}_3\text{N}_4/\text{TiO}_2$ composites as the content of melamine in the precursors decreased. The quenching is attributed to the charge transfer from $\text{g-C}_3\text{N}_4$ to TiO_2 , implying the increment in the separation efficiency of photoinduced electron-hole pairs. Although the PL intensity of CNT3 was slightly higher than that of the CNT1, it was much weaker than

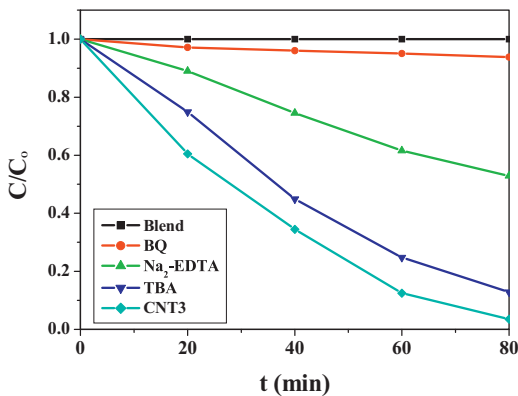


Fig. 14. Active species trapping experiments of the CNT3 heterojunction photocatalyst under visible light irradiation.

that of the pure g-C₃N₄ and CNT4. Therefore, it is not difficult to explain that the CNT3 sample exhibits an enhanced photocatalytic performance towards decomposition of RhB.

3.10. Possible photocatalytic degradation process

In the photocatalytic reaction process, some active species, such as superoxide radicals (•O₂⁻), holes (h⁺) and hydroxyl radicals (•OH) are generated by visible light irradiation. In order to further understand the photocatalytic mechanism of g-C₃N₄/TiO₂ composites, it is necessary to identify which reactive species play an important role in g-C₃N₄/TiO₂ composites for photodecomposition of RhB under visible light irradiation. In the present work, p-benzoquinone (p-BQ), disodium ethylenediaminetetraacetate (Na₂-EDTA) and tert-butyl alcohol (TBA) were used as scavengers for superoxide radicals (•O₂⁻), photoexcited holes (h⁺) and hydroxyl radicals (•OH), respectively [31,40]. As shown in Fig. 14, the photocatalytic performance of RhB obviously decreased when p-BQ and Na₂-EDTA were added, suggesting •O₂⁻ and h⁺ were the main reactive species for the decomposition of RhB. The addition of TBA had a weaker influence on the photodecomposition process of RhB, implying that •OH played a relatively minor role in RhB photodecomposition.

Usually, the high efficiency of charge separation in the heterojunction photocatalysts is a crucial factor for the significant enhancement of photocatalytic performance. However, whether it is effective to separate photoinduced charge carriers depends on the appropriate band edge positions of the two photocatalysts, because the band structure is responsible for the valid separation process of the electrons and holes [47]. The suitable band structure alignment of these semiconductors can generate space charge accumulation/depletion at the interfaces, which improves the separation efficiency of photoexcited electron-hole pairs [59]. The valence band (VB) and conduction band (CB) edge potentials of g-C₃N₄ and TiO₂ at the point of zero charge (pHzpc) can be predicted by the following empirical Eqs. (2) and (3):

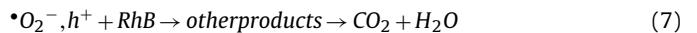
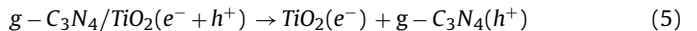
$$E_{VB} = \chi - E^e + 1/2E_g \quad (2)$$

$$E_{CB} = E_{VB} - E_g \quad (3)$$

where E_{CB}, E_{VB} and E_g are CB edge potential, VB edge potential and bandgap of the semiconductor, respectively. χ is the Sanderson electronegativity defined as the geometric mean of the electronegativity of the constituent atoms. E^e is the energy of free electrons on the hydrogen scale (4.5 eV vs NHE). The χ of TiO₂ and g-C₃N₄ are 5.81 and 4.73 eV, respectively. Based on the DRS results and Eqs. (2) and (3), the E_{CB} of TiO₂ and g-C₃N₄ were -0.31, -1.17 eV vs NHE,

respectively, while the E_{VB} of TiO₂ and g-C₃N₄ were 2.93, 1.63 eV vs NHE, respectively.

Based on the abovementioned experiment results, a reasonable mechanism for the enhanced photoactivity was proposed by promoting the charge transfer efficiency at the g-C₃N₄/TiO₂ interface, and schematically illustrated in Fig. 15. In the case of the single photocatalyst, g-C₃N₄ could be activated under 420 nm visible light irradiation (energy less than 2.95 eV) and generated electrons and holes. Unfortunately, the photogenerated electron-hole pairs in g-C₃N₄ recombined easily due to the narrow energy gap, and only a fraction of them involved in the photodegradation process, leading to a relative low activity [60]. In addition, the anatase TiO₂ could not be excited under 420 nm visible light irradiation because of broader band gap ($E_g = 3.24$ eV), thereby exhibiting a weaker photocatalytic activity. For g-C₃N₄/TiO₂ composite with an optimal g-C₃N₄ content, i.e. CNT3, g-C₃N₄ nanoparticles deposited on the surface of the macro-mesoporous TiO₂ particles, resulting in the formation of the heterostructure between g-C₃N₄ and TiO₂. Some of the electrons on g-C₃N₄ nanoparticles could transfer easily to CB of TiO₂ through the intimate interface because the conduction edge potential of g-C₃N₄ (-1.17 eV vs NHE) was lower than that of TiO₂ (-0.31 eV vs NHE). Many researchers also demonstrated that the differences in the CB edge potentials between g-C₃N₄ and TiO₂ were probably a more powerful driving force, which promoted electron flow from g-C₃N₄ to TiO₂ nanoparticles [61–63]. Meanwhile, photoexcited holes (h⁺) could tend to keep in the VB of g-C₃N₄. Namely, the CB of TiO₂ acts as a sink for photogenerated electrons in the present system thereby promoting efficiently the separation of photoinduced electron-hole pairs on the g-C₃N₄ particle surfaces. Since the CB levels of g-C₃N₄ and TiO₂ were more negative than the reduction potential of oxygen E° (O₂/^{*}O₂⁻) (-0.046 eV vs NHE) [64], as a result, the electrons on the CB of both g-C₃N₄ and TiO₂ could be taken up by O₂ adsorbed on the surface of the catalyst to generate •O₂⁻ radical species. Compared with the potential of •OH/H₂O (2.68 eV vs NHE) and •OH/OH⁻ (1.99 eV vs NHE) [65], the remained h⁺ on the VB of C₃N₄ could not react with OH⁻ or H₂O to generate •OH radicals because of the lower VB level of g-C₃N₄ (1.63 eV vs NHE). Subsequently, the highly reactive radical species •O₂⁻ and h⁺ participated in the photodecomposition of the RhB aqueous solution. The active species trapping experiment results also confirmed that •O₂⁻ and h⁺ were the main reactive species, •OH was the less critical one for the decomposition of RhB. The major reaction process in this photodegradation RhB mechanism under visible light irradiation were described as follows:



Consequently, it is not surprising that the g-C₃N₄/TiO₂ heterojunction photocatalysts exhibited much higher photocatalytic performance than pure g-C₃N₄ or TiO₂. In addition, it is also important to control prudently the content of g-C₃N₄ in g-C₃N₄/TiO₂ composites. An optimal content of g-C₃N₄ would improve the separation ability of photogenerated charge carriers, while excessive g-C₃N₄ (e.g. CNT4) may tend to form recombination center and block the electrons transferring from the g-C₃N₄ to TiO₂, thereby imposing a negative impact on the corresponding photocatalytic activity. As a consequence, it was not difficult to understand that the CNT3 heterojunction photocatalysts possessed the significant photocatalytic performance toward decomposition RhB under visible light irradiation.

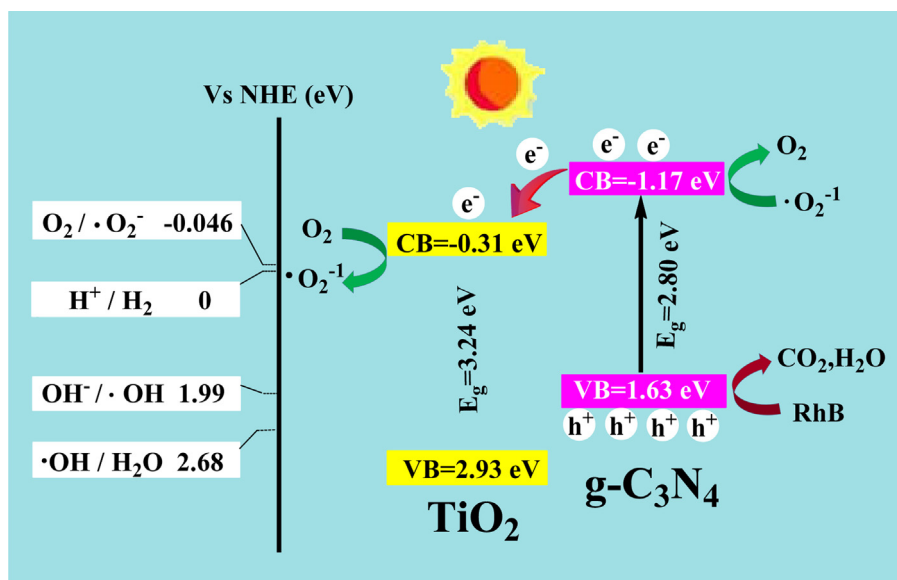


Fig. 15. Schematic diagrams photocatalytic mechanism of the CNTx heterojunction photocatalysts under visible light irradiation.

4. Conclusion

In conclusion, a series of macro/mesoporous CNTx heterojunction photocatalysts with intimated interface contact were successfully prepared by a facile calcination method using tetra-butyl titanate and melamine as the feedstocks. The content of g-C₃N₄ in the heterojunction photocatalysts had an important influence on the photocatalytic activity toward decomposition RhB under visible light irradiation. At the optimal g-C₃N₄ content, the as-prepared CNT3 sample exhibited the highest photocatalytic performance, exceeding that of pure TiO₂ and g-C₃N₄ by a factor of 7.2 and 3.1 respectively. The enhanced photocatalytic performance was ascribed to the fact that the CNT3 sample possessed a narrow band gap, a large BET specific surface area and an excellent heterostructure. The active species trapping experiments results demonstrated that superoxide radicals (•O₂⁻) and holes (h⁺) were main active species in the decomposition of RhB. A reasonable mechanism for the enhanced photoactivity was proposed by promoting the charge transfer efficiency at the g-C₃N₄/TiO₂ interface. This work may provide a new insight for the smart design and synthesis of various highly efficient photocatalysts for environmental and energy applications.

Acknowledgement

This work was financially supported by National Natural Science Foundation of China (51302112).

References

- [1] W.G. Wang, J.G. Yu, Q.J. Xiang, B. Cheng, Appl. Catal. B: Environ. 119 (2012) 109.
- [2] A.M. Yu, G.Q. Lu, J. Drennan, I.R. Gentle, Adv. Funct. Mater. 17 (2007) 2600.
- [3] L.L. Sun, G.H. Wang, R.R. Hao, D.Y. Han, S. Cao, Appl. Surf. Sci. 358 (2015) 91.
- [4] G.H. Wang, L. Xu, J. Zhang, T.T. Yin, D.Y. Han, Int. J. Photoenergy 2012 (2012) (265760).
- [5] S. Inturi, M. Suidan, P.G. Smirniotis, Appl. Catal. B: Environ. 180 (2016) 351.
- [6] Y.C. Pu, G.M. Wang, K.D. Chang, Y.C. Ling, Y.K. Lin, B.C. Fitzmorris, C.M. Liu, X.H. Lu, Y.X. Tong, J.Z. Zhang, Y.J. Hsu, Y. Li, Nano Lett. 13 (2013) 3817.
- [7] G.H. Wang, B. Cheng, J. Zhang, L. Xu, T.T. Yin, Int. J. Photoenergy 2012 (2012) 976389.
- [8] S.M. Wang, D.L. Li, C. Sun, S.G. Yang, Y. Guan, H. He, Appl. Catal. B: Environ. 144 (2014) 885.
- [9] S.A. Ansari, M.M. Khan, M.O. Ansari, M.H. Cho, Solar Energy Mater. Solar Cells 141 (2015) 162.
- [10] Z.C. Lian, W.C. Wang, S.N. Xiao, X. Li, Y.Y. Cui, D.Q. Zhang, G.S. Li, H.X. Li, Sci. Rep. UK 5 (2016) 10461, <http://dx.doi.org/10.1038/srep10461>.
- [11] Y. Wang, J.G. Yu, W. Xiao, Q. Li, J. Mater. Chem. A 2 (2014) 3847.
- [12] L. Sun, J.L. Zhai, H.Y. Li, Y. Zhao, H.J. Yang, H.W. Yu, ChemCatChem 6 (2014) 339.
- [13] J.R. Chen, F.X. Qiu, Y. Zhang, J.Z. Liang, H.J. Zhu, S.S. Cao, Appl. Surf. Sci. 356 (2015) 553.
- [14] K. Kondo, N. Murakami, C. Ye, T. Tsubota, T. Ohno, Appl. Catal. B: Environ. 142–143 (2013) 362.
- [15] L.Y. Mao, Y.R. Wang, Y.J. Zhong, J.Q. Ning, Y. Hu, J. Mater. Chem. A 1 (2013) 8101.
- [16] Z.F. Jiang, D.L. Jiang, Z.X. Yan, D. Liu, K. Qian, J.M. Xie, Appl. Catal. B: Environ. 170–171 (2015) 195.
- [17] X.B. Luo, F. Deng, L.J. Min, S.L. Luo, B. Guo, G.S. Zeng, C. Au, Environ. Sci. Technol. 47 (2013) 7404.
- [18] J. Xu, G.X. Wang, J.J. Fan, B.S. Liu, S.W. Cao, J.G. Yu, J. Power Sources 274 (2015) 77.
- [19] J.B. Mu, B. Chen, M.G. Zhang, Z.C. Guo, P. Zhang, C.L. Shao, Y.C. Liu, ACS Appl. Mater. Interfaces 4 (2012) 424.
- [20] L. Lin, Y.C. Yang, L. Men, X. Wang, D.N. He, Y.C. Chai, B. Zhao, S. Ghoshroy, Q.W. Tang, Nanoscale 5 (2013) 588.
- [21] Y.J. Lee, M.P. Jong, R. Jansen, Appl. Phys. Lett. 96 (2010) 082506.
- [22] D. Yang, Y.Y. Sun, Z.W. Tong, Y. Tian, Y.B. Li, Z.Y. Jiang, J. Phys. Chem. C 119 (2015) 5827.
- [23] R.J. Wang, G.H. Jiang, Y.W. Ding, Y. Yin, X.K. Sun, X.H. Wang, W.X. Chen, ACS Appl. Mater. Interfaces 3 (2011) 4154.
- [24] J.X. Low, S.W. Cao, J.G. Yu, S. Wageh, Chem. Commun. 50 (2014) 10768.
- [25] J.G. Yu, J.X. Low, W. Xiao, P. Zhou, M. Jaroniec, J. Am. Chem. Soc. 136 (2014) 8839.
- [26] D.L. Jiang, J.J. Zhu, M. Chen, J.M. Xie, J. Colloid Interface Sci. 417 (2014) 115.
- [27] X.J. Bai, L. Wang, Y.J. Wang, W.Q. Yao, Y.F. Zhu, Appl. Catal. B: Environ. 152–153 (2014) 262.
- [28] Y. Zheng, L.H. Lin, B. Wang, X.C. Wang, Angew. Chem. Int. Ed. 54 (2015) 12868.
- [29] S.W. Cao, J.X. Low, J.G. Yu, M. Jaroniec, Adv. Mater. 27 (2015) 2150.
- [30] H.T. Ren, S.Y. Jia, Y. Wu, S.H. Wu, T.H. Zhang, X. Han, Ind. Eng. Chem. Res. 53 (2014) 17645.
- [31] J.D. Xiao, Y.B. Xie, H.B. Cao, Y.Q. Wang, Z.J. Zhao, Catal. Commun. 66 (2015) 10.
- [32] H.G. Yu, F.Y. Chen, F. Chen, X.F. Wang, Appl. Surf. Sci. 358 (2015) 385.
- [33] D.J. Martin, K.P. Qiu, S.A. Shevlin, A.D. Handoko, J.W. Tang, Angew. Chem. 126 (2014) 9394.
- [34] Y.W. Zhang, J.H. Liu, G. Wu, W. Chen, Nanoscale 4 (2012) 5300.
- [35] G.Y. Li, X. Nie, Y.P. Gao, T.C. An, Appl. Catal. B: Environ. 180 (2016) 726.
- [36] M.J. Muñoz-Batista, A. Kubacka, M. Fernández-García, Catal. Sci. Technol. 4 (2014) 2006.
- [37] J.Y. Lei, Y. Chen, F. Shen, L.Z. Wang, Y.D. Liu, J.L. Zhang, J. Alloy Compd. 631 (2015) 328.
- [38] M.Q. Zang, L. Shi, L. Liang, D.F. Li, J.M. Sun, RSC Adv. 5 (2015) 56136.
- [39] K. Li, S.M. Gao, Q.Y. Wang, H. Xu, Z.Y. Wang, B.B. Huang, Y. Dai, J. Lu, ACS Appl. Mater. Interfaces 7 (2015) 9023.
- [40] L. Gu, J.Y. Wang, Z.J. Zou, X.J. Han, J. Hazard. Mater. 268 (2014) 216.
- [41] L. Zhang, D.W. Jing, X.L. She, H.W. Liu, D.J. Yang, Y. Lu, J. Li, Z.F. Zheng, L.J. Guo, J. Mater. Chem. A 2 (2014) 2071.
- [42] H.Q. Wang, J.Z. Li, C.C. Ma, Q.F. Guan, Z.Y. Lu, P.W. Huo, Y.S. Yan, Appl. Surf. Sci. 329 (2015) 17.

- [43] Z.A. Huang, Q. Sun, K.L. Lv, Z.H. Zhang, M. Li, B. Li, *Appl. Catal. B: Environ.* 164 (2015) 420.
- [44] J.G. Yu, Y.R. Su, B. Cheng, *Adv. Funct. Mater.* 17 (2007) 1984.
- [45] J.G. Yu, S.H. Wang, J.X. Low, W. Xiao, *Phys. Chem. Chem. Phys.* 15 (2013) 16883.
- [46] F. Chang, J. Zhang, Y.C. Xie, J. Chen, C.L. Li, J. Wang, J.R. Luo, B.Q. Deng, X.F. Hu, *Appl. Surf. Sci.* 311 (2014) 574.
- [47] J.G. Yu, J.R. Ran, *Energy Environ. Sci.* 4 (2011) 1364.
- [48] G.H. Dong, W. Ho, Y.H. Li, L.Z. Zhang, *Appl. Catal. B: Environ.* 174 (2015) 477.
- [49] K.S.W. Sing, D.H. Everett, R.A.W. Haul, L. Moscou, R.A. Pierotti, J. Rouquerol, T. Siemieniewska, *Pure Appl. Chem.* 57 (1985) 603.
- [50] J.G. Yu, Y.F. Yu, P. Zhou, W. Xiao, B. Cheng, *Appl. Catal. B: Environ.* 156–157 (2014) 184.
- [51] F. Dong, Z.W. Zhao, T. Xiong, Z.L. Ni, W.D. Zhang, Y.J. Sun, W.K. Ho, *ACS Appl. Mater. Interfaces* 5 (2013) 11392.
- [52] Y.F. Chen, W.X. Huang, Y. Situ, H. Huang, *ACS Appl. Mater. Interfaces* 6 (2014) 14405.
- [53] S.C. Yan, Z.S. Li, Z.G. Zou, *Langmuir* 26 (2010) 3894.
- [54] D.Y. Fu, G.Y. Han, F.F. Liu, Y.M. Xiao, H.F. Wang, R.Q. Liu, C.X. Liu, *Mater. Sci. Semicond. Proc.* 27 (2014) 966.
- [55] J.G. Yu, G.H. Wang, B. Cheng, M.H. Zhou, *Appl. Catal. B: Environ.* 69 (2007) 171.
- [56] H. Wang, X.Z. Yuan, Y. Wu, G.M. Zeng, X.H. Chen, L.J. Leng, H. Li, *Appl. Catal. B: Environ.* 174 (2015) 445.
- [57] J.D. Zhuang, W.X. Dai, Q.F. Tian, Z.H. Li, L.Y. Xie, J.X. Wang, P. Liu, *Langmuir* 26 (2010) 9686.
- [58] M. Sun, Q. Yan, T. Yan, M.M. Li, D. Wei, Z.P. Wang, Q. Wei, B. Du, *RSC Adv.* 4 (2014) 31019.
- [59] F. Jiang, T.T. Yan, H. Chen, A.W. Sun, C.M. Xu, X. Wang, *Appl. Surf. Sci.* 295 (2014) 164.
- [60] L.Y. Huang, H. Xu, Y.P. Li, H.M. Li, X.N. Cheng, J.X. Xia, Y.G. Xu, G.B. Cai, *Dalton Trans.* 42 (2013) 8606.
- [61] Y.X. Yang, Y.N. Guo, F.Y. Liu, X. Yuan, Y.H. Guo, S.Q. Zhang, W. Guo, M.X. Huo, *Appl. Catal. B: Environ.* 142–143 (2013) 828.
- [62] Y.P. Zang, L.P. Li, Y.S. Xu, Y. Zuo, G.S. Li, *J. Mater. Chem. A* 2 (2014) 15774.
- [63] S.W. Cao, J.G. Yu, *J. Phys. Chem. Lett.* 5 (2014) 2101.
- [64] B. Chai, T.Y. Peng, J. Mao, K. Li, L. Zan, *Phys. Chem. Chem. Phys.* 14 (2012) 16745.
- [65] Y.M. He, L.H. Zhang, B.T. Teng, M.H. Fan, *Environ. Sci. Technol.* 49 (2015) 649.